13

Toward TW-Peak-Power Single-Cycle IR Fields for Attosecond Physics and High-Field Science

O. D. Mücke[1], S. Ališauskas[1,2], A. J. Verhoef[1], A. Pugžlys[1], A. Baltuška[1], V. Smilgevičius[2], J. Pocius[3], L. Giniūnas[3], R. Danielius[3], and N. Forget[4]

[1]*Photonics Institute, Vienna University of Technology, Gusshausstrasse 27-387, A-1040 Vienna,*

[2]*Laser Research Center, Vilnius University, Saulėtekio av. 10, LT-10223 Vilnius,*

[3]*Light Conversion Ltd., P/O Box 1485, Saulėtekio av. 10, LT-10223 Vilnius,*

[4]*Fastlite, Bâtiment 403, Ecole Polytechnique, FR-91128 Palaiseau,*

[1]*Austria*

[2,3]*Lithuania*

[4]*France*

1. Introduction

Optical Parametric Chirped-Pulse Amplification (OPCPA) (Dubietis et al., 1992, 2006) has attracted a lot of attention as a promising route toward intensity scaling of few-cycle laser pulses. Intense carrier-envelope phase (CEP)-stable few-cycle laser pulses have numerous intriguing applications in attosecond and high-field science (for a recent review, see Krausz & Ivanov, 2009) including the production of attosecond XUV/soft-X-ray pulses by high-harmonic generation (HHG) (Hentschel et al., 2001; Kienberger et al., 2004; Sansone et al., 2006), tomographic imaging of molecular orbitals (Itatani et al., 2004), and laser-induced electron diffraction (Meckel et al., 2008). A major challenge for using HHG in studies of time-resolved tomography of molecular dissociative states is the low ionization potential I_p of excited molecular states. The resulting competition between state depletion and HHG prevents generation of broad HHG spectra necessary for tomographic reconstruction. One solution are laser sources with high ponderomotive energy $U_p \propto \lambda^2 I$ at moderate intensity level, i.e., infrared (IR) CEP-stable few-cycle high-power laser systems. The present immense interest of the ultrafast community in high-U_p-sources (Fuji et al., 2006; Vozzi et al., 2006, 2007, 2009; Takahashi et al., 2008a, 2008b; Gu et al., 2009; Mücke et al., 2009a, 2009b; Moses et al., 2009) has three major reasons:

(1) These sources open the door to previously inaccessible regimes of light-matter interactions (Blaga et al., 2009) and in particular they allow experimental investigations of the λ-scaling laws of strong-field physics (Tate et al., 2007; Colosimo et al., 2008; Agostini & DiMauro, 2008; Doumy et al., 2009) (Keldysh parameter $\propto\lambda^{-1}$, electron energies $\propto\lambda^2$, HHG cutoff $\propto\lambda^2$, minimum attosecond pulse duration $\propto\lambda^{-1/2}$). In addition, e.g., laser-induced electron diffraction experiments would benefit from IR driving because of the shorter de Broglie electron wavelength and consequently higher spatial resolution (Meckel et al., 2008).

Source: Advances in Solid-State Lasers: Development and Applications, Book edited by: Mikhail Grishin, ISBN 978-953-7619-80-0, pp. 630, February 2010, INTECH, Croatia, downloaded from SCIYO.COM

(2) Because of the λ^2-dependence of the HHG cutoff (Sheehy et al., 1999; Shan & Chang, 2001; Gordon & Kärtner, 2005), HHG driven by intense few-cycle IR sources holds great promise for the realization of bright coherent sources in the soft- and potentially even hard-X-ray region (Popmintchev et al., 2009). The achievable HHG photon fluence depends both on the microscopic single-atom response of the gas and on macroscopic effects in the gas target like phase matching and absorption. Currently, both microscopic and macroscopic parts are subject of a heated scientific debate. While the majority of studies (Tate et al., 2007; Schiessl et al., 2007; Colosimo et al., 2008) proclaimed a $\lambda^{-(5\text{-}6)}$-scaling of the single-atom HHG conversion efficiency or even worse (Shiner et al., 2009), Frolov et al. (2009) (also compare Pérez-Hernández et al., 2009) argued that the energy-dependence of the atomic photo-recombination cross-section and irregularities in the photoionization cross-section (e.g., originating from Cooper minima or electron correlation effects) can lead to more favorable HHG efficiency scaling ($\propto\lambda^{-5.3}$ for H, $\propto\lambda^{-4.6}$ for He, and $\propto\lambda^{-3.9}$ for Ar) and in some cases (e.g., in Xe) even to an increase of the HHG efficiency with increasing λ. Concerning macroscopic effects, recent work on phase matching of higher harmonics driven by high-energy IR pulses (Yakovlev et al., 2007; Popmintchev et al., 2008, 2009; Takahashi et al., 2008a, 2008b; Falcão-Filho et al., 2009) indicate the feasibility to compensate the sharp drop of the microscopic HHG efficiency macroscopically by an increased optimal gas pressure for phase matching and a strongly decreasing reabsorption of the generated X-rays at higher photon energies.

(3) The development of high-U_p-sources is also of paramount importance for attosecond photoelectron spectroscopy of solid surfaces and surface-adsorbate systems (Cavalieri et al., 2007; Miaja-Avila et al., 2008). Applying the experimental techniques of attosecond science to solid surfaces is very challenging and significantly more difficult than gas-phase experiments because the solid target is not continuously replaced (like in a gas jet), the target density can not be varied (e.g., to reduce space-charge effects), and detection of ions as well as using them as observable is impossible. Nevertheless, Cavalieri et al. (2007) have recently demonstrated that the attosecond ponderomotive streaking technique can be extended to solid surfaces in a narrow intensity window: space-charge effects originating from above-threshold ionization (ATI) electrons cause a severe background problem if the few-cycle driver pulse intensity is too high. If, on the other hand, the intensity is too low, the ponderomotive streaking is too small to be observed. For a maximum acceptable intensity determined by the experimental conditions (e.g., damage threshold of the solid target, background problems from space-charge effects), IR high-U_p-sources are superior to 0.8-µm Ti:sapphire sources because they exhibit stronger ponderomotive streaking effects.

For many applications in attosecond science, in particular for the generation of isolated attosecond XUV/soft-X-ray pulses, extremely short pulses comprising only one or two light oscillations underneath the field envelope are required. The well-established standard technology for the generation of few-cycle driver pulses is spectral broadening of mJ-level femtosecond pulses from Ti:sapphire amplifier systems in noble gases. Using 5-fs 1-mJ 720-nm driver pulses obtained in this way, coherent X-rays in the keV photon energy range were demonstrated by HHG in He (Seres et al., 2005). At present, the energy throughput of gas-phase broadening schemes, such as the hollow-core fiber compressor (Nisoli et al., 1996, 1997) and filamentation (Hauri et al., 2004, 2007), is limited to 4-5 mJ at 0.8 µm due to ionization losses. In filamentation of intense femtosecond pulses, a self-guiding channel ("filament") is formed due to the dynamical balance between self-focusing by the nonlinear Kerr effect and defocusing by the plasma created by gas ionization. During the nonlinear pulse propagation, the spectrum is significantly broadened by the Kerr nonlinearity and

plasma-induced blue-shifting. Since no waveguiding structure is required in filamentation and therefore coupling losses are eliminated, the filamentation technique permits higher energy throughput than the hollow-core fiber compressor. With IR pulses we expect to surpass the present energy limitation for gas broadening schemes since the critical power of self-focusing scales as λ^2 (Bergé, 2008).

In this chapter we present a hybrid IR OPCPA/filamentation approach to pursue a TW-peak-power single-cycle IR source that will find many applications in attosecond and high-field science. The chapter is organized as follows: In section 2, we provide the theoretical background of optical parametric amplification (OPA) with special emphasis on Type-II phase matching in KTP crystals, as employed in our IR OPCPA. In section 3, a CEP-stable 10-mJ-class four-stage OPCPA system at 1.5 μm is discussed in detail. In section 4, we present experiments on spectral broadening and self-compression of multi-mJ 1.5-μm pulses via filamentation in noble gases.

2. Type-II optical parametric amplification in KTP crystals

In ultrafast parametric amplifiers (Cerullo & De Silvestri, 2003), an intense pump beam of high frequency ω_p is used to amplify a signal and an idler beam with frequencies ω_s and ω_i ($\omega_p > \omega_s > \omega_i$), respectively:

$$\omega_p = \omega_s + \omega_i \,. \tag{1}$$

The signal ω_s lies within $\omega_p/2$ and ω_p, the corresponding idler within $\omega_p/2$ ("degeneracy") and 0. In addition to the energy conservation (1), for an efficient energy transfer in the parametric interaction also the corresponding momenta of the pulses, $k_j = 2\pi n_j/\lambda_j$ (j=p,s,i), must be conserved ("phase matching"):

$$\vec{k}_p = \vec{k}_s + \vec{k}_i \quad \Leftrightarrow \quad \Delta\vec{k} = \vec{k}_p - \vec{k}_s - \vec{k}_i = 0 \,. \tag{2}$$

The phase matching condition (2) cannot be fulfilled in bulk isotropic materials in the normal dispersion region ($n_p > n_s > n_i$). However, phase matching can be achieved in birefringent crystals taking advantage of the different refractive indices of the ordinary (o) and extraordinary (e) beams. Depending on the polarizations of the pump, signal and idler beams, one distinguishes different types of phase matching. For example, Table 1 illustrates three different types of phase matching in the crystallographic XZ-plane in KTP (Liu et al., 2001).

phase-matching type	γ_{sp}	γ_{si}
Type I ($e_s + e_i \rightarrow o_p$)	2/3	2
Type II ($e_s + o_i \rightarrow o_p$)	2/3	2/3
Type III ($o_s + e_i \rightarrow o_p$)	2	2/3

Table 1. OPA phase-matching types in the XZ-plane in the biaxial crystal KTP and corresponding cross-phase modulation (XPM) coupling coefficients γ_{sp} and γ_{si}

In general, phase matching can be achieved by angle-tuning the nonlinear crystal, i.e., by adjusting the polar θ-angle and azimuthal φ-angle, or by changing the crystal temperature.

Type-I OPAs feature ultrabroadband phase matching and gain, especially for operation near the degeneracy point, $\omega_s = \omega_i = \omega_p/2$ (Cerullo & De Silvestri, 2003). For this reason, Type-I

phase matching has been extremely popular for the generation of ultrashort pulses and high-energy few-cycle driver pulses for attosecond physics and high-field science. The experiences made with these systems during the past few years, however, have also revealed some severe drawbacks inherent to Type-I phase matching:

- Type-I parametric amplification of CEP-stable two-cycle IR seed pulses obtained from difference-frequency generation (DFG) to the energy level close to 1 mJ has been demonstrated (Fuji et al., 2006; Vozzi et al., 2006, 2007; Gu et al., 2009; Moses et al., 2009). However, the inherently low DFG seed energy causes a sizable superfluorescence background (Fuji et al., 2006; Gu et al., 2009; Moses et al., 2009) that prevents further energy upscaling.
- Type-I OPAs exhibit ultrabroadband phase matching, but vice versa they are also negatively optimized for back-conversion into the pump.
- Even though Type-I OPAs deliver output spectra with FWHM bandwidth in excess of 200 nm, the quality of the resulting compressed pulses most often remains poor due to intrinsically steep slopes of the parametrically amplified spectra.
- Near-degenerate Type-I OPAs have the worst possible quantum defect for the signal wave (i.e., half of the pump photon energy is "lost" with the idler).
- When scaling up the pulse energies to the millijoule-level, (cascaded) four-wave mixing (FWM) can lead to problems due to parasitic self-diffraction (Beržanskis et al., 1995; Varanavičius et al., 1997).

For these reasons, we decided to pursue a hybrid Type-II OPCPA/filamentation scheme to realize a TW-peak-power single-cycle IR source. By employing more narrowband Type-II phase matching, one can optimize the spectral brightness of the seed at the expense of the seed energy, achieve a more uniform saturation across the pulse spectrum, minimize energy back-conversion into the pump, and minimize self-diffraction. Following the pioneering work of Kraemer et al. (2006, 2007), we employ Type-II KTP (1.030/1.064 µm pump, ~1.5 µm signal, ~3.3-3.7 µm idler) because these crystals are transparent for the mid-IR idler wavelength and exhibit a relatively broad bandwidth around 1.5 µm.

$KTiOPO_4$ (KTP) and $KTiOAsO_4$ (KTA) are biaxial crystals permitting Type-II ($e_s + o_i \rightarrow o_p$) phase matching in the crystallographic XZ-plane (i.e., φ=0°): the o-beam propagates into the y-direction, $n_o=n_y$, the e-beam parallel to the XZ-plane, $n_x<n_e<n_z$, with

$$n_e(\theta) = n_x \frac{\sqrt{1+\tan^2\theta}}{\sqrt{1+\left(n_x/n_z\right)^2\tan^2\theta}}. \tag{3}$$

For noncollinear Type-II ($e_s + o_i \rightarrow o_p$) phase matching, where α is the (internal) noncollinearity angle between the pump and signal beams inside the crystal and β the resulting angle between pump and idler satisfying Eq. (2), the analysis by Liu et al. (2001) yields the relations

$$\frac{n_y^{\mathrm{p}}}{\lambda_{\mathrm{p}}} = \frac{n_z^{\mathrm{s}}}{\lambda_{\mathrm{s}}}\cos\alpha + \frac{n_y^{\mathrm{i}}}{\lambda_{\mathrm{i}}}\cos\beta \tag{4}$$

$$\beta = \arcsin\left(\frac{\lambda_{\mathrm{i}}}{\lambda_{\mathrm{p}}}\frac{n_y^{\mathrm{p}}}{n_y^{\mathrm{i}}}\sin\alpha\right) - \alpha \tag{5}$$

from which the optimum phase-matching angle θ_{pm} can be determined

$$\sin\theta_{\mathrm{pm}} = \frac{n_z^{\mathrm{s}}}{\dfrac{n_y^{\mathrm{p}}}{\lambda_{\mathrm{p}}}\cos\alpha - \dfrac{n_y^{\mathrm{i}}}{\lambda_{\mathrm{i}}}\cos(\alpha+\beta)} \sqrt{\frac{\left(\dfrac{n_x^{\mathrm{s}}}{\lambda_{\mathrm{s}}}\right)^2 - \left(\dfrac{n_y^{\mathrm{p}}}{\lambda_{\mathrm{p}}}\cos\alpha - \dfrac{n_y^{\mathrm{i}}}{\lambda_{\mathrm{i}}}\cos(\alpha+\beta)\right)^2}{\left(n_x^{\mathrm{s}}\right)^2 - \left(n_z^{\mathrm{s}}\right)^2}}. \tag{6}$$

Eq. (5) reflects the angular dispersion of the idler for noncollinear (i.e., $\alpha \neq 0$) phase matching. Using the Sellmeier equations summarized in the Appendix for computing the refractive index components of KTP, the above equations can readily be evaluated. Fig. 1(a) depicts the resulting theoretical angle-tuning curves.

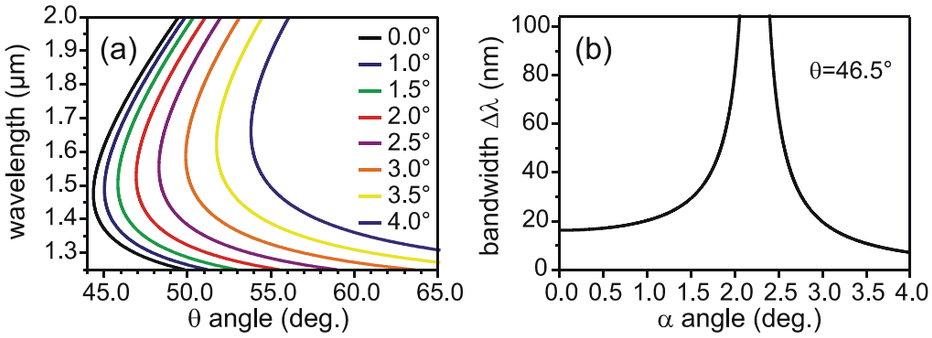

Fig. 1. Noncollinear Type-II ($e_{\mathrm{s}} + o_{\mathrm{i}} \rightarrow o_{\mathrm{p}}$) phase matching in KTP for λ_{p}=1.064 μm: (a) Signal wavelength versus phase-matching angle θ for various (internal) noncollinearity angles α as indicated. (b) Parametric FWHM phase-matching bandwidth $\Delta\lambda$ [computed from Eq. 8(a)] versus noncollinearity angle α for θ=46.5°, L=10 mm, and λ_{s}=1.55 μm. Signal-idler group-velocity matching is achieved for $\alpha_{\mathrm{si}} \approx 2.2°$. At this point, Eq. 8(a) loses its applicability.

The broadest phase-matching bandwidth can be achieved in an OPA, when the group velocities (GV) of signal and idler pulses $v_{\mathrm{s,i}}=(\partial k_{\mathrm{s,i}}/\partial\omega)^{-1}$ are matched [see Fig. 1(b)]. In case of perfect group-velocity matching, the maximum phase-matching bandwidth is then determined by the mismatch of the group-velocity dispersion (GVD) of signal and idler pulses, $\mathrm{GVD}_{\mathrm{s,i}}=(\partial^2 k_{\mathrm{s,i}}/\partial\omega^2)$. The signal-idler group-velocity mismatch (GVM)

$$\frac{1}{\mathrm{GVM}_{\mathrm{si}}} = \frac{1}{v_{\mathrm{i}}\cos(\alpha+\beta)} - \frac{1}{v_{\mathrm{s}}} \tag{7}$$

can be controlled by varying the noncollinearity angle α, and the parametric FWHM gain bandwidth can be calculated from

$$\Delta\lambda = \begin{cases} \dfrac{\lambda_{\mathrm{s}}^2 \left|\mathrm{GVM}_{\mathrm{si}}\right|}{c_0 L} & \text{for} \quad \dfrac{1}{\mathrm{GVM}_{\mathrm{si}}} \neq 0 \qquad (8a) \\ \dfrac{0.8\lambda_{\mathrm{s}}^2}{c_0\sqrt{\left|\mathrm{GVDM}_{\mathrm{si}}\right| L}} & \text{for} \quad \dfrac{1}{\mathrm{GVM}_{\mathrm{si}}} = 0 \qquad (8b) \end{cases}$$

with the vacuum velocity of light c_0, crystal length L, and signal-idler GVD mismatch $GVDM_{si}$ (Liu et al. (2001)). The optimum (internal) angle for signal-idler group-velocity matching can also directly be obtained from the expression (Cerullo & De Silvestri, 2003)

$$\alpha_{si} = \arcsin\left(\frac{1 - v_s^2 / v_i^2}{1 + 2v_s n_s \lambda_i / v_i n_i \lambda_s + n_s^2 \lambda_i^2 / n_i^2 \lambda_s^2}\right)^{1/2}. \tag{9}$$

For θ=46.5°, λ_p=1.064 µm and λ_s=1.55 µm, Eq. (9) predicts a value of α_{si} =2.2°.
The parametric gain G can be calculated from the coupled equations describing parametric processes (Cerullo & De Silvestri, 2003). If the OPA is seeded with a small light intensity I_{s0} at the signal wavelength only (i.e., I_{i0}=0) and neglecting pump depletion (i.e., pump intensity I_p=const.), the solution of the coupled equations are

$$I_s(L) = I_{s0}\left[1 + \frac{\Gamma^2}{g^2}\sinh^2(gL)\right] \xrightarrow{\Gamma L \gg 1} I_s(L) \approx \frac{1}{4} I_{s0} \exp(2gL) \tag{10a}$$

$$I_i(L) = I_{s0}\frac{\lambda_s}{\lambda_i}\frac{\Gamma^2}{g^2}\sinh^2(gL) \xrightarrow{\Gamma L \gg 1} I_i(L) \approx \frac{1}{4}\frac{\lambda_s}{\lambda_i} I_{s0} \exp(2gL) \tag{10b}$$

where the formulas on the right-hand side give the limit for large gains. In Eqs. (10) we used the gain coefficients defined as

$$g = \sqrt{\Gamma^2 - (\Delta k/2)^2}\ , \text{ with } \Gamma^2 = \frac{8\pi^2 d_{eff}^2}{n_p n_s n_i \lambda_s \lambda_i \varepsilon_0 c_0} I_p \tag{11}$$

with the permittivity of vacuum ε_0. The effective nonlinear optical coefficient d_{eff} of KTP for Type-II phase-matching in the XZ-plane is (Dmitriev et al., 1999)

$$d_{eff} = d_{32} \sin\theta\ , \text{ with } d_{32}(1.064\,\mu\text{m}) = 2.65\,\text{pm/V}\ . \tag{12}$$

From Eqs. (10), we see that the parametric gain G is given by

$$G = 1 + \frac{\Gamma^2}{g^2}\sinh^2(gL) \xrightarrow{\Gamma L \gg 1} G \approx \frac{1}{4}\exp(2gL)\,. \tag{13}$$

Fig. 2 shows the theoretical gain spectrum calculated for the experimental conditions in our booster-amplification stage 4 (see Figs. 8 and 9, Table 2). Note, however, that for the high intensities in our OPCPA stage 4, pump depletion cannot be ignored which results in a reduced gain in the experiment.
In our discussion, we so far have neglected spatial effects. However, the energy transfer in the parametric interaction is limited by the Poynting vector walk-off between the pump, signal and idler pulses. For KTP, the (internal) angle between pump and signal beams, for which Poynting vector walk-off is compensated, is given by (Dmitriev et al., 1999)

$$\rho(\theta) = -\arctan[(n_o / n_e(\theta))^2 \tan\theta] + \theta\,. \tag{14}$$

For a Type-II (e_s + $o_i \rightarrow o_p$) KTP OPA pumped at 1.03 µm or 1.064 µm, the external walk-off compensation angle is 2.2°.

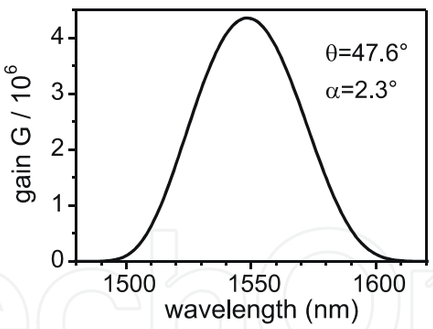

Fig. 2. Gain spectrum (pump depletion neglected) of a Type-II ($e_s + o_i \rightarrow o_p$) KTP OPA pumped at λ_p=1.064 μm. Pump intensity I_p=20 GW/cm², θ=47.6°, α=2.3°, and L=10 mm.

3. CEP-stable 10-mJ-class chirped parametric amplifier at 1.5 μm

In this section, we describe in detail a CEP-stable four-stage IR OPCPA system delivering 1.5-μm signal pulses (and corresponding idler pulses at ~3.3-3.7 μm) with up to 12.5 mJ pulse energy before recompression. This IR OPCPA is based on a CEP-stable two-stage OPA seed source discussed in subsection 3.1 and two booster-amplification stages presented in subsection 3.2.

3.1 CEP-stable 4-μJ OPA seed source

The scheme of our two-stage OPA seed source is depicted in Fig. 3.

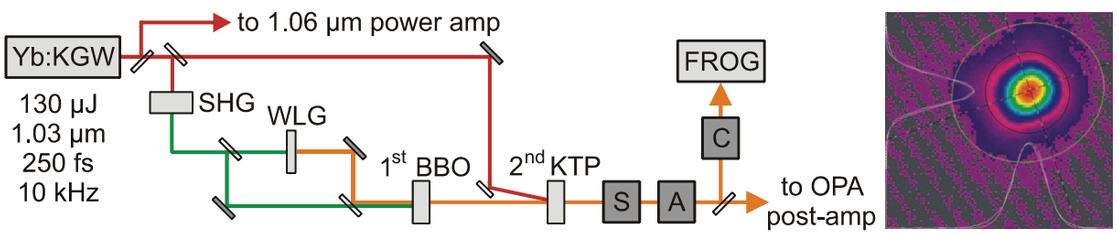

Fig. 3. Scheme of the CEP-stable two-stage 1.5-μm OPA seed source. Yb:KGW, 250 fs Yb:KGW MOPA system; SHG, second-harmonic generation in BBO; WLG, white-light generation in sapphire; S/C, grating stretcher/compressor; A, acousto-optic programmable dispersive filter (DAZZLER). Right panel, far-field beam profile of second-stage signal wave.

In our IR OPCPA scheme (see Figs. 3 and 8), both Yb:KGW and Nd:YAG regenerative amplifiers (RAs) are simultaneously seeded from a single Yb:KGW master oscillator that has a modest FWHM bandwidth of 30 nm centered at 1.04 μm [see Fig. 4(a)]. To seed the Nd:YAG RA, we pick up unused 1064-nm light behind a transmission grating in the pulse stretcher of the Yb:KGW MOPA. The repetition rate of the Yb:KGW diode-pumped solid state (DPSS) MOPA (Pharos, Light Conversion, Ltd.), tunable in the range of 1-100 kHz, was set at 10 kHz as the 500th harmonic of the flash-lamp-pumped Nd:YAG amplifier (Ekspla Ltd.) operating at 20 Hz. In the Nd:YAG RA, an intracavity etalon is used to narrow the pulse bandwidth and make the pulse duration safe for post amplification [see Fig. 4(b)].

The 1.03-μm output from the femtosecond Yb:KGW MOPA is first split into two parts by means of a variable beam splitter (consisting of a half-wave plate and a thin-film polarizer);

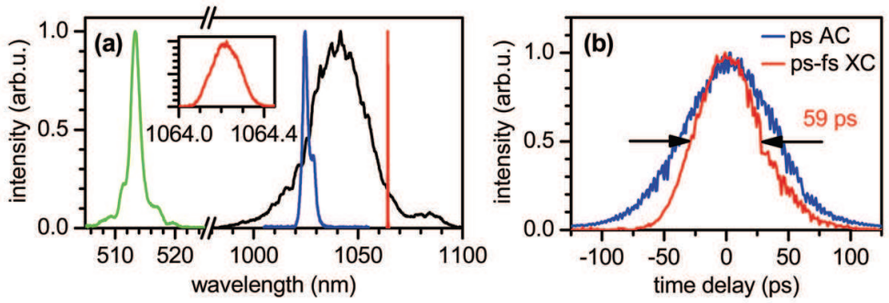

Fig. 4. Optical synchronization of the Yb:KGW and Nd:YAG amplifiers. (a) Laser spectra: Kerr-lens mode-locked Yb:KGW oscillator (black curve), Yb:KGW regenerative amplifier (blue), Nd:YAG with an intracavity 2-mm thick etalon (red), and SHG of Yb:KGW RA (green). (b) Pulse measurement of the ps Nd:YAG amplifier showing an autocorrelation (AC, blue) and a cross-correlation (XC, red) between the Yb:KGW (250 fs) and Nd:YAG.

part one is used for implementing the first OPA stage, part two is used for pumping the second OPA stage. In the first OPA stage, the 1.03-µm pulses are first frequency-doubled in a 1-mm thick Type-I BBO crystal (θ=23.4°, φ=90°). Typically 8.5 µJ of 515-nm pulses are again split by a variable beam splitter into two parts: 1.3 µJ (measured behind a variable aperture used for fine-adjusting the input beam diameter) are focused onto a 10-mm thick sapphire plate using an 87-mm focusing lens. In the sapphire plate, a stable white-light (WL) continuum extending to wavelengths >840 nm [see Fig. 5(a)] is created in a single filament. For a sapphire plate thickness of 10 mm we obtain a stronger and more stable WL seed at >780 nm than for thinner plates of 4–6 mm. The WL continuum, which is recollimated with a 40-mm lens, is used to seed the first OPA stage. The WL seed pulses and the 515-nm pump pulses are combined collinearly [i.e., α=0° to avoid angular dispersion of the idler, compare Eq. (5)] on a dichroic beam splitter and both are focused onto a 4-mm thick Type-I BBO crystal (θ=22.8°, φ=90°) with an f=20 cm spherical mirror to a $1/e^2$ pump beam diameter of 120 µm. In the pump beam, a variable aperture is used to adjust the pump energy to 1.4 µJ (thus, the parametric gain) and to minimize the detrimental effects of amplified spontaneous emission (ASE). By adjusting both the θ-angle of the BBO crystal and time delay between the seed and pump pulses, different wavelength regions can be phase matched for efficient parametric amplification [Fig. 5(a)]. In particular, selecting the ~795 nm wavelength for amplification, this configuration produces CEP-stable idler pulses (Baltuška et al., 2002) at 1.44 µm [see Fig. 5(b)] that we use as a seed in the second OPA stage.

Following the pioneering work of Kraemer et al. (2006, 2007), we employ Type-II KTP crystals (1.03/1.064 µm pump, ~1.5 µm signal, ~3.3-3.7 µm idler) for the subsequent OPA stages 2-4 because these crystals (unlike borate crystals) are transparent for the mid-IR idler wavelength and exhibit a relatively broad bandwidth around 1.5 µm. The CEP-stable idler pulses from the first OPA stage are recollimated with a 10-cm lens and focused onto a 6-mm thick Type-II KTP crystal (θ=45.5°, φ=0°) using a 50-cm lens. The pump beam is focused onto the same KTP crystal using a 100-cm lens under an (external) walk-off compensation angle of 2.2° with respect to the seed beam. For a pump beam diameter of ~550 µm measured at the KTP crystal input face and 69 µJ (measured behind a variable aperture) pump pulses, we achieve 4 µJ signal pulses, i.e., a pump-signal conversion efficiency of ~6%

in the second OPA stage. The pulse-to-pulse intensity fluctuations of the two-stage OPA amounts to 2.5% rms noise, only two times larger than that of the Yb:KGW MOPA pump (1.2% rms). The far-field beam profile of the second-stage signal wave shown in Fig. 3 is nearly Gaussian; the beam propagation factor was determined to be M^2=1.13±0.04 as compared to M^2<1.2 of the Yb:KGW MOPA pump.

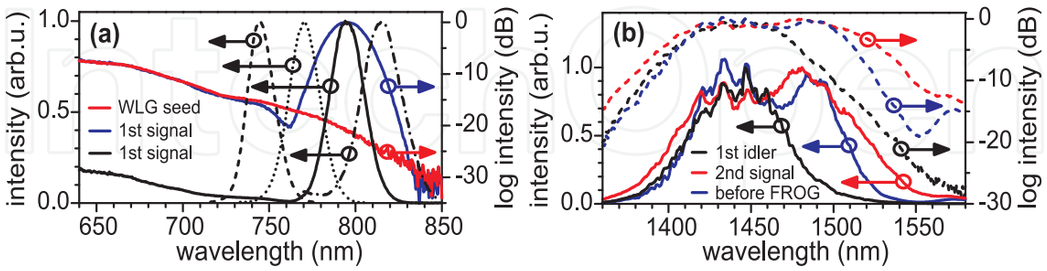

Fig. 5. Spectral properties of two-stage 1.5-µm OPA. (a) Near-IR WL seed (red) and signal spectra (blue and black solid) of the first OPA stage. The dashed and dotted curves indicate tunability of the first-stage signal (and corresponding idler). (b) Infrared passively CEP-stable seed (black), amplified second-stage signal (red), spectrum before FROG setup (blue). The amount of ASE is immeasurable in absence of the WL seed.

The strong nonlinear optical Kerr effect in KTP [nonlinear refractive index coefficient n_2(KTP) = 23.7×10^{-16} cm^2/W as compared to n_2(BBO) = 2.9×10^{-16} cm^2/W (Koechner, 2006)] raises the important question how severe is pump/idler-to-signal cross-phase modulation (XPM) in the second OPA stage and its effect on CEP stability. The nonlinear effects accumulated during the OPA process in a nonlinear crystal of length L can be quantified by introducing a generalized B-integral

$$B = \frac{2\pi n_2}{\lambda_s} \int_0^L \mathrm{d}z \left[I_s(z) + \gamma_{sp} I_p(z) + \gamma_{si} I_i(z) \right]. \tag{15}$$

The coefficients γ_{sp} and γ_{si} (see Table 1), which quantify the pump/idler-to-signal coupling, are 2 for parallel polarizations and 2/3 for orthogonal polarizations (Agrawal, 2007). Obviously, Type-II (e_s + o_i → o_p) phase matching as used in our amplification stages 2-4 minimizes the detrimental XPM contribution of pump and idler on the signal wave.

CEP stability of the OPA 2 output was studied by means of inline f-to-2f interferometry: a supercontinuum is generated by focusing the 1.5-µm pulses into a 3-mm thick sapphire plate with a 15-mm lens. After recollimation, the second harmonic of the 1.5-µm pulses is generated in a 0.2-mm thick Type-I BBO crystal (θ=19.8°, φ=90°). With a polarizer, the supercontinuum and SHG are projected onto a common axis and the resulting f-to-2f interferograms from 650 to 790 nm are recorded with a spectrometer (see Fig. 6). The observation of stable interference fringes directly proves CEP stability and negligible influence of XPM on the CEP. The slow CEP drift observed in Fig. 6 is clearly of an environmental origin and can easily be compensated for by feedback stabilization of the interferometer formed by the seed and pump paths in the first OPA stage (see Fig. 3).

In stand-alone applications of our two-stage OPA, the well-behaved spectral phase of the second-stage signal can readily be compensated for by highly reflective chirped mirrors. Here, keeping in mind mainly the development of a >10 mJ four-stage IR OPCPA system,

we instead demonstrate that the second-stage output can be stretched to ~40 ps and again recompressed to a sub-40-fs duration using a grating-based stretcher/compressor pair (Kalashnikov et al., 2005) employing 500 grooves/mm 96% efficient gold reflection gratings and an IR high-resolution acousto-optic programmable dispersive filter (DAZZLER) (Verluise et al., 2000).

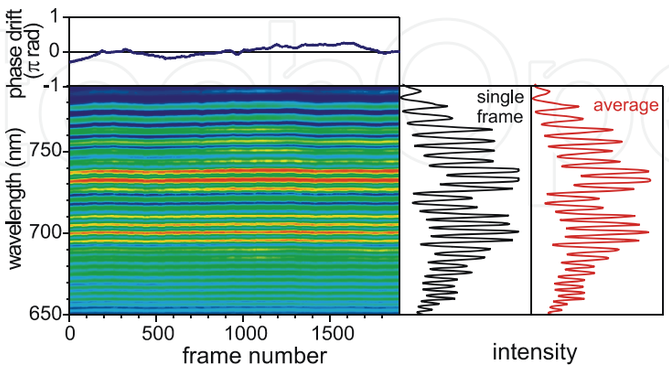

Fig. 6. *f*-to-2*f* interferograms exhibiting stable fringes due to CEP stability. The red and black curves on the right panels indicate the spectra averaged over 1900 frames (2 ms frame exposure time) and a single frame, respectively, on the same intensity axis. The blue curve in the above panel indicates the extracted phase drift of the second-stage signal.

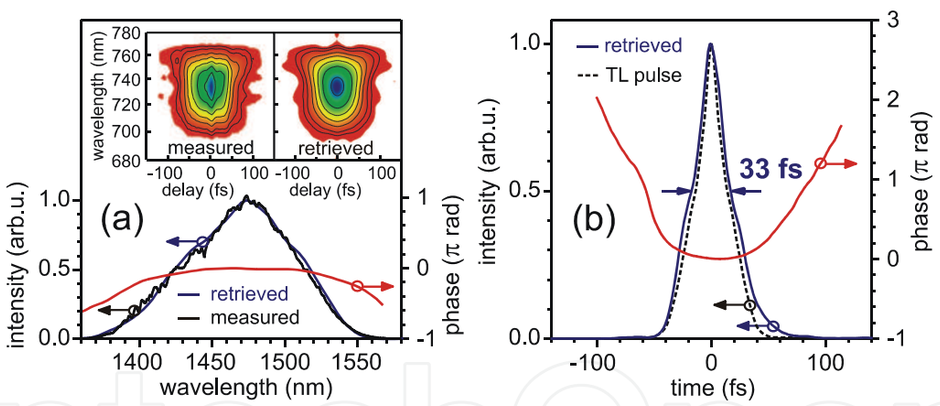

Fig. 7. SHG-FROG characterization of the stretched and recompressed 1.47-μm pulses: (a) Measured spectrum (black curve), retrieved spectral intensity (blue) and phase (red). The insets show the measured and retrieved FROG traces. (b) Retrieved temporal intensity (blue) and phase (red) profile indicating a 33-fs FWHM pulse duration. The transform-limited intensity profile (black dashed) corresponds to a 28-fs duration.

Fig. 7 shows SHG-frequency-resolved optical gating (FROG) measurements of 1.47-μm pulses with a 92-nm FWHM bandwidth from the second OPA stage after stretching to ~40 ps and recompression to a 33-fs FWHM pulse duration.

Our parametric infrared source, easily tunable in the 1.5-1.6 μm range, might find applications in pump-probe experiments on InAs quantum dot semiconductor optical amplifiers (QD SOAs) operating in the 1.55-μm telecommunications wavelength range (Zilkie et al., 2006) or for buried-waveguide writing in semiconductors based on three-photon absorption (Nejadmalayeri et al., 2005).

3.2 Power-amplification to pulse energies exceeding 10 mJ

In the subsequent booster-amplification stages 3 and 4 shown in Fig. 8, the 1.5-μm signal pulses are amplified from the 4-μJ level to energies >10 mJ before recompression.

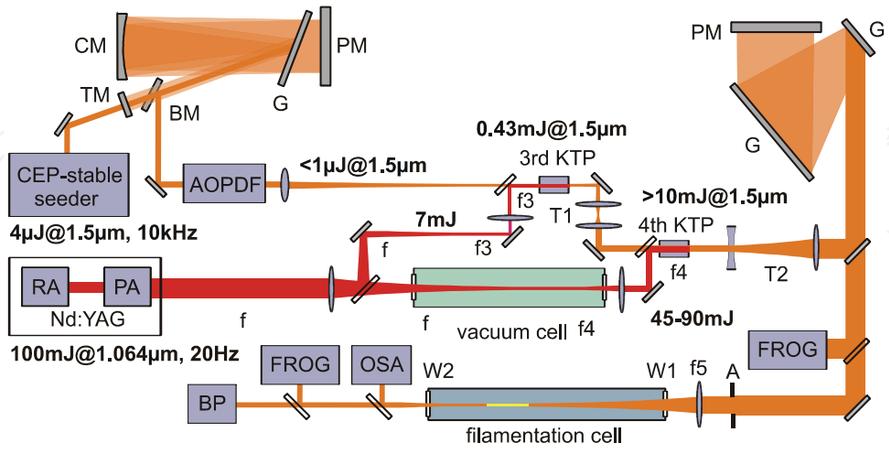

Fig. 8. Scheme of the OPCPA power-amplification stages 3 and 4: G, reflection grating; CM, curved mirror; PM, plane mirror; TM/BM, top/bottom mirror; AOPDF, acousto-optic programmable dispersive filter; RA, regenerative amplifier; PA, double-pass post amplifier; f, f3, f4, f5, lens focal lengths; T1, T2, telescopes; A, iris aperture; W1/W2, input/output windows; OSA, optical spectrum analyzer; BP, beam profiler (pyroelectric 2D array).

As already mentioned in the previous subsection, in order to optimize the energy extraction from the 60-ps long Nd:YAG pump pulses, the passively CEP-stable 1.5-μm pulses from the front-end are temporally stretched to ~40 ps using a grating-based stretcher. In addition, a high-resolution IR DAZZLER is used for higher-order dispersion control. To guarantee a homogeneous pump profile free of hot spots, we relay-image the 10-mm-diameter crystal rod in the Nd:YAG power amplifier onto the 10-mm thick KTP crystals in stages 3 and 4. The measured surface damage threshold of KTP for our pump pulses (21 GW/cm^2) determines a pump spot diameter of 2 mm and 3.1 mm for stages 3 and 4, respectively. Relay-imaging is achieved with three lenses with focal lengths of f=75 cm, f3=10 cm, and f4=35 cm (see Fig. 8). Because of the larger pump intensities in the fourth OPA stage, the focus needs to be placed inside a vacuum cell to avoid a breakthrough in air. The 1.5-μm (seed) pulses are focused onto the third-stage KTP crystal with a 750-mm lens and imaged onto the fourth-stage KTP crystal with telescope T1. The (external) walk-off compensation angle between the pump and seed beams is 2.2°. With this pumping geometry and ~90 mJ pump pulses, we have achieved up to 12.5 mJ signal pulses centered at 1.57 μm with a pump-signal conversion efficiency of ~22% in the final OPCPA stage. To avoid damage to the gold gratings in the OPCPA compressor, we expand the beam diameter of the fourth-stage output by a factor of 5 to 9.5 mm (at the 1/e^2-level) by means of a Galilean beam expander T2.

The spectra of the seed and amplified signal pulses of the power-amplification stages are shown in Fig. 9. In principle, saturating the OPCPA stages permits amplification of pulses with nearly 80 nm bandwidth corresponding to a Fourier limit of ~65 fs. As idler absorption increases above 3.4 μm in KTP, we can achieve higher output powers when tuning the signal center wavelength above 1.55 μm. The SHG-FROG characterization data of 3.5-mJ

1.57-μm pulses with 62 nm bandwidth from the 20-Hz four-stage IR OPCPA (see Fig. 10) indicate a 74.4-fs FWHM pulse duration, close to the transform limit (TL) of 72.6 fs. Ultimately, with further optimization sub-70-fs pulse durations seem in reach by recompressing pulses with bandwidths approaching 80 nm.

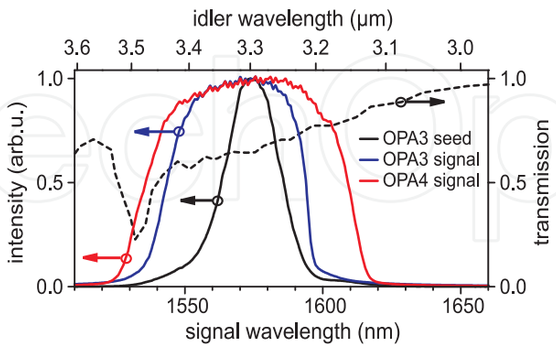

Fig. 9. Spectral properties of the power-amplification OPCPA stages: spectrum of the third-stage seed, amplified signal spectra after stages 3 and 4. The amount of superfluorescence is immeasurable in absence of the WL seed in OPA stage 1. The dashed curve indicates the idler transmission through 10 mm of KTP.

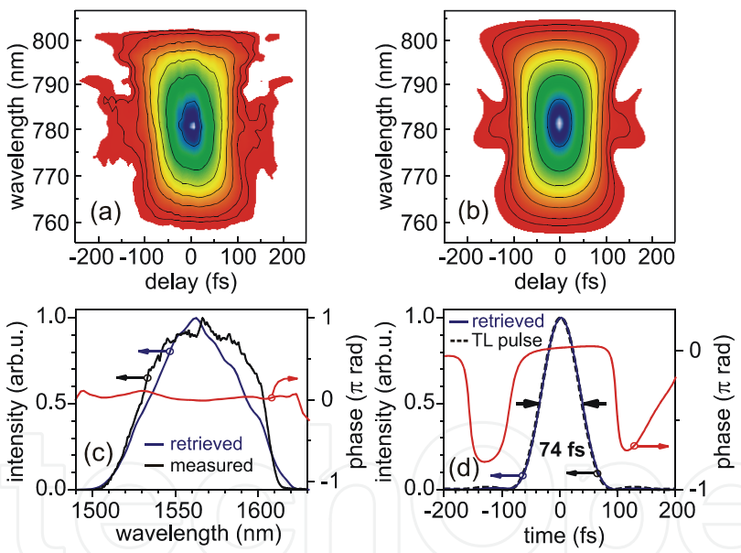

Fig. 10. SHG-FROG characterization of the 20-Hz output from the four-stage IR OPCPA: (a) Measured and (b) retrieved FROG traces. (c) Measured spectrum (back curve), retrieved spectral intensity (blue) and phase (red). (d) Retrieved temporal intensity (blue) and phase (red) profiles exhibiting a 74.4-fs FWHM pulse duration. The TL intensity profile (dashed) corresponds to a 72.6-fs duration.

Concerning the CEP stability of our four-stage IR OPCPA, there are in principle three sources of CEP instabilities:

i. Possible superfluorescence backgrounds can compromise the CEP stability on short time scales. Since superfluorescence is well-suppressed in our IR OPCPA, this effect is expected to be negligible.

ii. On a longer (say, second) time scale, the CEP can drift due to slow environmental relative path-length changes of pump and seed arms in the first OPA stage [see Fig. (3)]. At the moment, we are implementing a feedback stabilization of these path-length drifts to remove slow CEP drifts from the four-stage IR OPCPA output.

iii. As already discussed in subsection 3.1, the CEP stability could in principle also be compromised by amplitude-to-phase-noise conversion due to pump/idler-to-signal XPM in OPA stages 2-4. The importance of this effect can readily be estimated by the generalized *B*-integral defined in Eq. (15). Here, ignoring the less intense idler wave and assuming a constant pump intensity over the crystal length L=10 mm, Eq. (15) simplifies to

$$B = \frac{2\pi n_2}{\lambda_s} L \gamma_{sp} I_p \,. \tag{16}$$

From this equation, the XPM-induced CEP noise $\Delta\phi_{CE,rms}$ can be estimated assuming 2% rms intensity fluctuations of the Nd:YAG pump amplifier. The results of this estimate summarized in Table 2 indicate that amplitude-to-phase-noise conversion due to XPM is completely negligible in OPA stages 3 and 4. Thus, the output of the four-stage IR OPCPA inherits the excellent short-term CEP stability of the two-stage OPA front-end.

	OPA3	OPA4
pump pulse energy	7 mJ	90 mJ (maximum)
pump diameter	2 mm	3.1 mm
pump intensity	3.7 GW/cm²	20 GW/cm²
B	0.02 π	0.11 π
$\Delta\phi_{CE,rms}$	4×10^{-4} π	2.2×10^{-3} π

Table 2. Estimate for XPM-induced CEP noise $\Delta\phi_{CE,rms}$ in OPA stages 3 and 4.

4. Spectral broadening and pulse self-compression via filamentation in noble gases

In this section, we demonstrate single-filament IR supercontinuum generation via femtosecond filamentation in noble gases. Depending on the experimental conditions, two filamentation regimes can be achieved: (i) the filamentation regime without plasma-induced pulse self-recompression, as discussed in section 4.1, and (ii) the self-compression regime, as discussed in section 4.2. Ultimately, since the critical power of self-focusing scales as λ^2, we expect to surpass the current energy limitation [4-5 mJ at 800 nm (Suda et al., 2005; Stibenz et al., 2006)] with the multi-mJ femtosecond pulses obtained from our IR OPCPA. In addition, a promising route for further pulse energy upscaling is the use of circularly/elliptically polarized input pulses (Trisorio & Hauri, 2007; Varela, 2009).

4.1 Multimillijoule filamentation without plasma-induced pulse self-compression

In the filamentation experiments (see Fig. 8), the 1.57-μm OPCPA pulses were focused using a 50-cm lens placed 4 cm in front of the AR-coated input window W1 of a 138-cm long gas cell filled with argon (I_p=15.76 eV) or krypton (I_p=13.99 eV) at the absolute pressure of 4-5 bar.

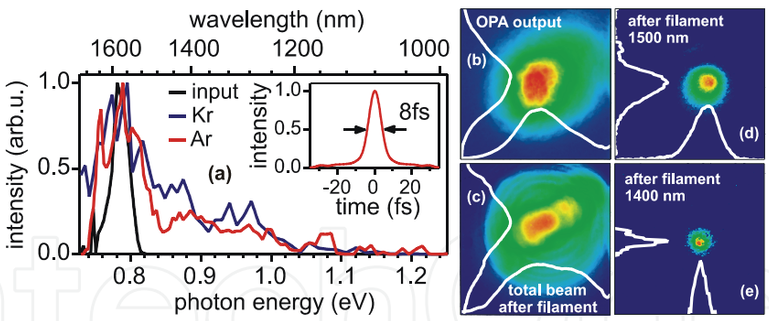

Fig. 11. (a) Filamentation of 1.57-µm pulses in noble gases: Individually normalized input (black curve) and output spectra for filamentation of 0.8-mJ pulses in krypton (blue) and 2.5-mJ pulses in argon (red) at a 5-bar pressure. The inset shows the TL intensity profile computed from the argon output spectrum. (b)-(e) Far-field spatial beam profiles measured with the pyroelectric 2D array: (b) before the OPCPA grating compressor; (c) total (frequency-unresolved) beam profile behind the Ar cell; (d) beam profile at 1500 nm; (e) beam profile at 1400 nm. (d) and (e) are taken at the same camera position as (c) by inserting narrowband filters into the beam. Image size is 12.4 mm×12.4 mm.

In the filamentation regime without plasma-induced pulse self-recompression (see Fig. 11), we generated ~3-mJ 600-nm-wide IR supercontinua of high spatial quality supporting 8-fs pulse durations, which corresponds to less than two optical cycles at 1.5 µm.

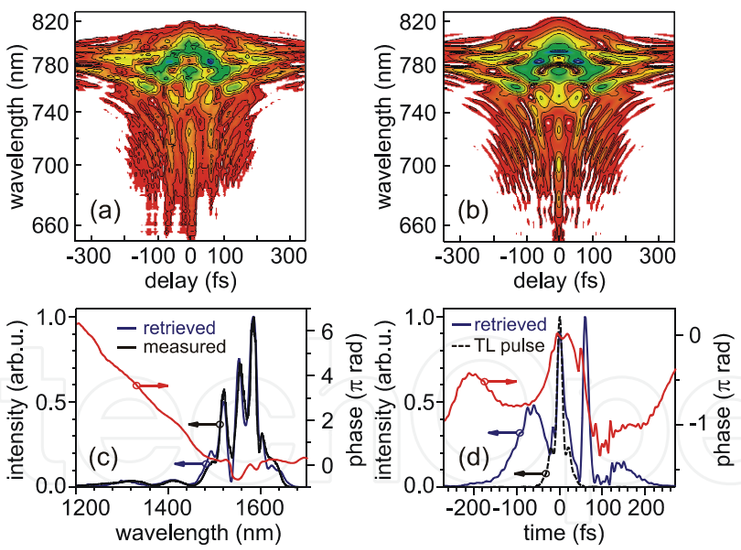

Fig. 12. SHG-FROG characterization of 2.1-mJ filamentation output pulses for argon at 4 bar: (a) Measured and (b) retrieved FROG traces. (c) Measured spectrum (black curve), retrieved spectral intensity (blue) and phase (red). (d) Retrieved temporal intensity (blue) and phase (red) profiles. The TL intensity profile (dashed) corresponds to a 14.6-fs duration.

SHG-FROG data of such spectrally broadened pulses are displayed in Fig. 12. We emphasize that the FROG characterization (Figs. 12 and 13) and corresponding output pulse energy measurements were performed without aperturing the filamentation output beam. In the experiment shown in Fig. 12, the input pulse energy was 3.0 mJ, output energy 2.1 mJ,

corresponding to an energy throughput of 68% including the 8% reflection losses on the uncoated 1-mm thick BK7 output window W2 (see Fig. 8). The SHG-FROG data reveal a rather complex spectro-temporal structure. The observed strong nonlinear phase leads to a temporal break-up into two peaks of 20 fs and 15 fs FWHM duration, separated by 60 fs. Since a clean single-filament spatial profile was observed simultaneously, we conclude that the temporal splitting apparently helps to keep the pulse intensity below the break-up threshold of a single filament. A more elaborate time-frequency analysis of these data employing Wigner distributions is presented in section 4.3.

4.2 Self-compression of millijoule infrared pulses

The filamentation regime involving plasma-induced pulse self-compression is particularly attractive for the pursuit of TW-peak-power single-cycle IR sources. Recently, Hauri et al. (2007) demonstrated that filamentation of rather long ~55-fs OPA pulses at 2 μm in a xenon cell allows the generation of self-compressed 17-fs 0.27-mJ pulses. The limited input pulse energy available in that experiment implied the use of xenon as a noble gas with the highest nonlinearity. Detailed numerical investigation of self-compression of 2-μm laser filaments (Bergé, 2008) predicted a number of highly attractive features of femtosecond filamentation at longer carrier wavelength λ: (i) The bandwidth of the generated supercontinuum increases with λ; (ii) for comparable ratios of input power over critical power, P_{in}/P_{crit}, filaments at IR wavelengths have higher pulse energy than near-VIS filaments; (iii) the filament channel extends over longer distances and its waist scales $\propto\lambda$; (iv) self-steepening becomes more pronounced with increasing λ; (v) for gases with moderate ionization potentials (I_p<20 eV, e.g., argon or xenon), the numerical calculations reveal that mid-IR filamentation easily permits self-compression to single-cycle pulse durations, as compared to self-compressed 2-3-cycle durations at visible wavelengths. Self-compression of 2-μm pulses resulted in supercontinua exhibiting a much flatter spectral phase over the full bandwidth as compared to 800-nm pulses. Bergé (2008) also made the important observation that for self-compression of 2-μm pulses, due to nonlinear pulse propagation the shortest achievable pulse duration survives only over shorter distances (~15-20 cm) in the gas medium as compared to the 800-nm case (~60 cm), i.e., the proper choice of the output window position with respect to the filament channel is crucial for observing optimum self-compression.

By lowering the input pulse energy and tuning the gas pressure in the cell, we achieved the regime of pulse self-compression. In the experiment shown in Fig. 13, CEP-stable 2.2-mJ 74.4-fs 1.57-μm input pulses are compressed in a single filament in argon down to a 19.8-fs duration. This represents a temporal compression of the input pulses by a factor of ~4. The output energy was 1.5 mJ, corresponding to the energy throughput of 66%, again including the 8% reflection losses on window W2. The IR supercontinuum with a 130-nm FWHM bandwidth originates from a 12-15-cm long filament. The low-intensity spectral wings of the supercontinuum extend throughout the VIS and are easily visible with the naked eye (see Fig. 14).

As argued above, careful optimization of the propagation distance in the pressurized argon cell behind the filament might lead to the observation of even shorter pulse durations (Bergé, 2008). In addition, the spectral phase is remarkably reproducible on a daily basis which holds potential for further recompression using fixed-dispersion chirped mirrors.

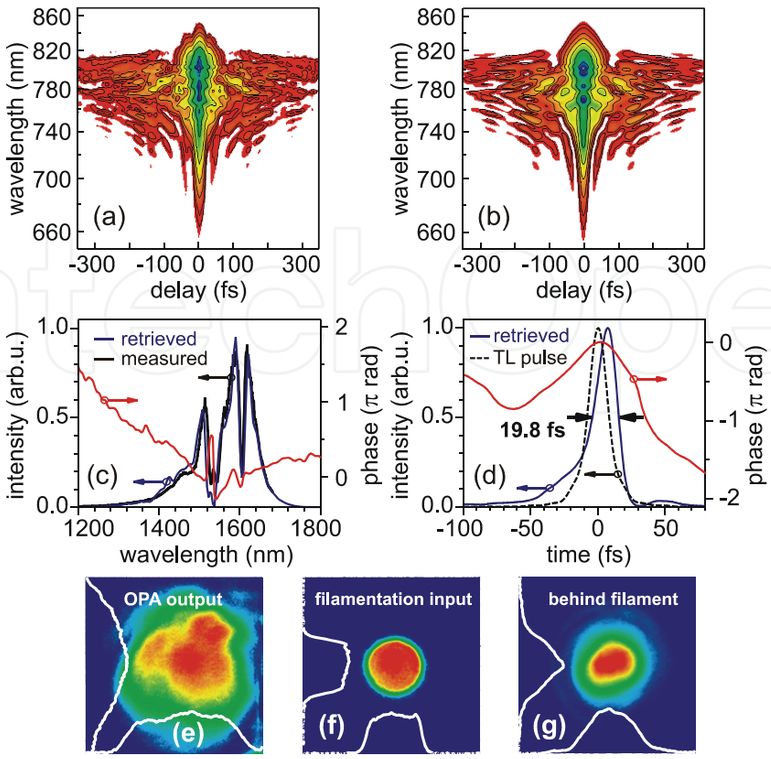

Fig. 13. Self-compression of 1.5-mJ pulses in argon at 5 bar: (a) Measured and (b) retrieved FROG traces. (c) Measured spectrum (black curve), retrieved spectral intensity (blue) and phase (red). (d) Retrieved temporal intensity (blue) and phase (red) profiles indicating a 19.8-fs pulse duration. The TL intensity profile (dashed) corresponds to a 15.9-fs duration. (e)-(g) Far-field spatial beam profiles measured with the pyroelectric 2D array: (e) after OPCPA grating compressor; (f) apertured filamentation input behind the iris aperture A; (g) total beam profile behind the filamentation cell. Image size is 12.4 mm×12.4 mm.

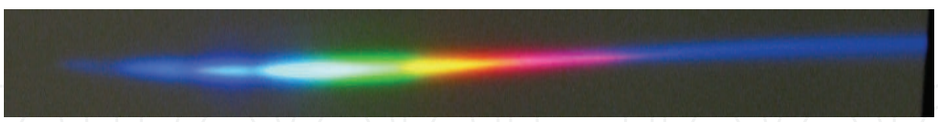

Fig. 14. Photo of the spectrally resolved filamentation output in the self-compression regime.

Concerning the CEP stability of the filamentation output, several femtosecond filamentation experiments performed at various center wavelengths (Hauri et al., 2004, 2007) have clearly demonstrated that the filamentation process preserves the CEP stability of the input pulses. Therefore, we are convinced that the filamentation process does not degrade the CEP stability of the OPCPA input pulses in our experiment. Nevertheless, in order to quantify the quality of CEP stability, we are planning (i) to perform inline *f*-to-2*f* interferometry to the OPCPA output of stages 3 and 4, (ii) quantify possible differential CEP drifts caused in the individual amplification stages 3 and 4 using a TADPOLE-type technique, (iii) and finally perform *f*-to-3*f* interferometry (since a sizable third harmonic is generated inside the filament) to the filamentation output.

4.3 Time-frequency analysis employing Wigner distributions

For the time-frequency analysis, it is very instructive to look at the Wigner distributions

$$W(t,\omega) = \int \mathrm{d}\tau\, E^*\left(t - \frac{\tau}{2}\right) E\left(t + \frac{\tau}{2}\right) \exp(\mathrm{i}\omega\tau) \tag{17}$$

directly computed from the FROG data (Paye, 1992). When integrating these 2D data over wavelength, one obtains the temporal intensity profile, while integration over time yields the pulse spectrum:

$$I(t) = \int \mathrm{d}\omega\, W(t,\omega) \text{ and } \tilde{I}(\omega) = \int \mathrm{d}t\, W(t,\omega) \tag{18}$$

The Wigner distribution functions extracted from the filamentation FROG data corresponding to the two distinct filamentation regimes are displayed in Fig. 15.

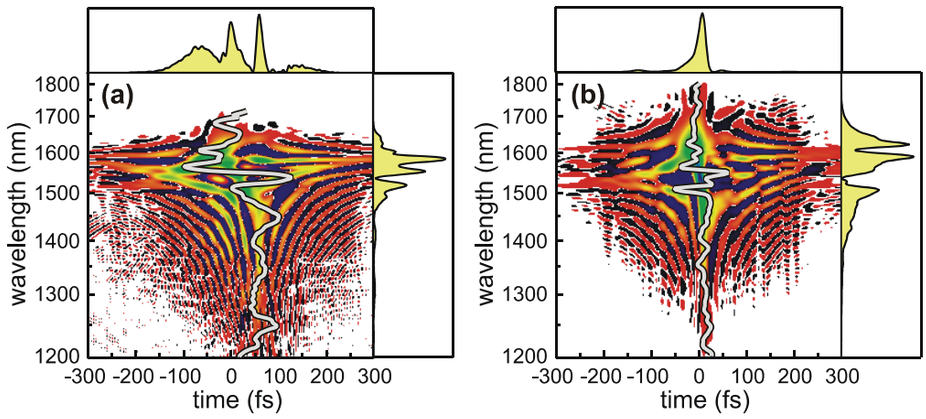

Fig. 15. Wigner distribution functions: (a) filamentation without self-compression extracted from the SHG-FROG data in Fig. 12, (b) self-compression result obtained from Fig. 13. The grey curves indicate the retrieved group delay (GD). The panels above and on the right indicate the temporal intensity profile and pulse spectrum, respectively.

Although the SHG-FROG traces in Figs. 12 and 13 look qualitatively rather different, the Wigner distributions now look more similar. The main difference is that in the self-compression regime [Fig. 15(b)], the group delay is much flatter and exhibits much smaller oscillations than the data obtained in the filamentation regime without self-compression [Fig. 15(a)]. The fact that both cases do not differ qualitatively gives us hope that the filamentation is in principle nicely scalable and that we can control it with further work.

5. Conclusions

In conclusion, we have demonstrated CEP-stable parametric amplification at 1.5 µm signal wavelength with pulse energies up to 12.5 mJ based on a fusion of a DPSS femtosecond Yb:KGW MOPA system and picosecond Nd:YAG solid-state technology. Moreover, we demonstrated multi-mJ IR supercontinuum generation as well as self-compression of CEP-stable 2.2-mJ 74.4-fs 1.57-µm input pulses down to 19.8 fs duration in a single filament in argon with 1.5-mJ output energy and a 66% energy throughput. The output energy was scaled up by 5.6 times over earlier results (Hauri et al., 2007). The output energy and energy

throughput can be further increased by systematically optimizing the experimental conditions (input pulse energy and beam diameter, focusing lens and position, gas type and pressure, input polarization, gas cell length etc.). Ultimately, with our 1.6-μm pulses we expect to surpass the present energy limitation [4-5 mJ at 800 nm (Suda et al., 2005; Stibenz et al., 2006)] for gas broadening schemes (Bergé, 2008).

6. Acknowledgments

This work has been supported by the Austrian Science Fund (FWF), grants U33-N16 and F1619-N08, LASERLAB-EUROPE II (JRA HAPPIE), and partly supported by the Lithuanian State Science and Studies Foundation (project No. B-42/2009). O. D. Mücke gratefully acknowledges support from a Lise-Meitner Fellowship by the FWF (project M1094-N14).

Appendix

Within the wavelength interval 0.5 μm < λ < 3.5 μm, the refractive index components of KTP can be evaluated using the Sellmeier equations

$$n_j^2 = A_j + B_j / (\lambda^2 - C_j) - D_j \lambda^2 \tag{A1}$$

with Sellmeier coefficients K_j (K=A,B,C,D and j=x,y,z)

	A	B	C	D
x	3.006700	0.039500	0.042510	0.012470
y	3.031900	0.041520	0.045860	0.013370
z	3.313400	0.056940	0.059410	0.016713

Table 3. Sellmeier coefficients for KTP according to Eq. (A1).

These Sellmeier equations (A1) and coefficients in Table 3 are recommended by C. Bonnin, Cristal Laser, http://www.cristal-laser.fr/prod_pdf/tech1.pdf, and are used for crystal type KTP_F in the SNLO version 41 nonlinear optics code available from A. V. Smith, Sandia National Laboratories, Albuquerque, NM 87185-1423.

7. References

Agrawal, G. P. (2007). *Nonlinear Fiber Optics,* 4th edition, Academic Press, ISBN 978-0-12-369516-1, New York

Agostini, P. & DiMauro, L. F. (2008), Atoms in high intensity mid-infrared pulses, *Contemp. Phys.* 49, 179-197

Baltuška, A., Fuji, T. & Kobayashi, T. (2002), Controlling the Carrier-Envelope Phase of Ultrashort Light Pulses with Optical Parametric Amplifiers, *Phys. Rev. Lett.* 88, 133901-1-4

Bergé, L. (2008), Self-compression of 2 μm laser filaments, *Opt. Express* 16, 21529-21543

Beržanskis, A., Danielius, R., Dubietis, A., Piskarskas, A. & Stabinis, A. (1995), Parametrically induced light diffraction in crystals with second-order susceptibility, *Appl. Phys. B* 60, 421-426

Blaga, C. I., Catoire, F., Colosimo, P., Paulus, G. G., Muller, H. G., Agostini, P. & DiMauro, L. F. (2009), Strong-field photoionization revisited, *Nature Phys.* 5, 335-338

Cavalieri, A. L., Müller, N., Uphues, T., Yakovlev, V. S., Baltuška, A., Horvath, B., Schmidt, B., Blümel, L., Holzwarth, R., Hendel, S., Drescher, M., Kleineberg, U., Echenique, P. M., Kienberger, R., Krausz, F. & Heinzmann, U. (2007), Attosecond spectroscopy in condensed matter, *Nature* 449, 1029-1032

Cerullo, G. & De Silvestri, S. (2003), Ultrafast optical parametric amplifiers, *Rev. Sci. Instrum.* 74, 1-18

Colosimo, P., Doumy, G., Blaga, C. I., Wheeler, J., Hauri, C., Catoire, F., Tate, J., Chirla, R., March, A. M., Paulus, G. G., Muller, H. G., Agostini, P. & DiMauro, L. F. (2008), Scaling strong-field interactions towards the classical limit, *Nature Phys.* 4, 386-389

Dmitriev, V. G., Gurzadyan, G. G. & Nikogosyan, D. N. (1999). *Handbook of Nonlinear Optical Crystals,* 3rd edition, Springer, ISBN 3-540-65394-5, Berlin

Doumy, G., Wheeler, J., Roedig, C., Chirla, R., Agostini, P. & DiMauro, L. F. (2009), Attosecond Synchronization of High-Order Harmonics from Midinfrared Drivers, *Phys. Rev. Lett.* 102, 093002-1-4

Dubietis, A., Jonušauskas, G. & Piskarskas, A. (1992), Powerful femtosecond pulse generation by chirped and stretched pulse parametric amplification in BBO crystal, *Opt. Commun.* 88, 437-440

Dubietis, A., Butkus, R. & Piskarskas, A. P. (2006), Trends in Chirped Pulse Optical Parametric Amplification, *IEEE J. Sel. Top. Quantum Electron.* 12, 163-172

Falcão-Filho, E. L., Gkortsas, V. M., Gordon, A. & Kärtner, F. X. (2009), Analytic scaling analysis of high harmonic generation conversion efficiency, *Opt. Express* 17, 11217-11229

Frolov, M. V., Manakov, N. L., Sarantseva, T. S., Emelin, M. Y., Ryabikin, M. Y. & Starace, A. F. (2009), Analytic Description of the High-Energy Plateau in Harmonic Generation by Atoms: Can the Harmonic Power Increase with Increasing Laser Wavelengths?, *Phys. Rev. Lett.* 102, 243901-1-4

Fuji, T., Ishii, N., Teisset, C. Y., Gu, X., Metzger, T., Baltuška, A., Forget, N., Kaplan, D., Galvanauskas, A. & Krausz, F. (2006), Parametric amplification of few-cycle carrier-envelope phase-stable pulses at 2.1 μm, *Opt. Lett.* 31, 1103-1105

Gordon, A. & Kärtner, F. X. (2005), Scaling of keV HHG photon yield with drive wavelength, *Opt. Express* 13, 2941-2947

Gu, X., Marcus, G., Deng, Y., Metzger, T., Teisset, C., Ishii, N., Fuji, T., Baltuska, A., Butkus, R., Pervak, V., Ishizuki, H., Taira, T., Kobayashi, T., Kienberger, R. & Krausz, F. (2009), Generation of carrier-envelope-phase-stable 2-cycle 740-μJ pulses at 2.1-μm carrier wavelength, *Opt. Express* 17, 62-69

Hauri, C. P., Kornelis, W., Helbing, F. W., Heinrich, A., Couairon, A., Mysyrowicz, A., Biegert, J. & Keller, U. (2004), Generation of intense, carrier-envelope phase-locked few-cycle laser pulses through filamentation, *Appl. Phys. B* 79, 673–677

Hauri, C. P., Lopez-Martens, R. B., Blaga, C. I., Schultz, K. D., Cryan, J., Chirla, R., Colosimo, P., Doumy, G., March, A. M., Roedig, C., Sistrunk, E., Tate, J., Wheeler, J., DiMauro, L. F. & Power, E. P. (2007), Intense self-compressed, self-phase-stabilized few-cycle pulses at 2 μm from an optical filament, *Opt. Lett.* 32, 868-870

Hentschel, M., Kienberger, R., Spielmann, C., Reider, G. A., Milosevic, N., Brabec, T., Corkum, P., Heinzmann, U., Drescher, M. & Krausz, F. (2001), Attosecond metrology, *Nature* 414, 509-513

Itatani, J., Levesque, J., Zeidler, D., Niikura, H., Pépin, H., Kieffer, J. C., Corkum, P. B. & Villeneuve, D. M. (2004), Tomographic imaging of molecular orbitals, *Nature* 432, 867-871

Kalashnikov, M. P., Risse, E., Schönnagel, H. & Sandner, W. (2005), Double chirped-pulse-amplification laser: a way to clean pulses temporally, *Opt. Lett.* 30, 923-925

Kienberger, R., Goulielmakis, E., Uiberacker, M., Baltuska, A., Yakovlev, V., Bammer, F., Scrinzi, A., Westerwalbesloh, T., Kleineberg, U., Heinzmann, U., Drescher, M. & Krausz, F. (2004), Atomic transient recorder, *Nature* 427, 817-821

Koechner, W. (2006). *Solid-State Laser Engineering,* 6th edition, Springer, ISBN 978-0387-29094-2, Berlin

Kraemer, D., Hua, R., Cowan, M. L., Franjic, K. & Miller, R. J. D. (2006), Ultrafast noncollinear optical parametric chirped pulse amplification in KTiOAsO4, *Opt. Lett.* 31, 981-983

Kraemer, D., Cowan, M. L., Hua, R., Franjic, K. & Miller, R. J. D. (2007), High-power femtosecond infrared laser source based on noncollinear optical parametric chirped pulse amplification, *J. Opt. Soc. Am. B* 24, 813-818

Krausz, F. & Ivanov, M. (2009), Attosecond physics, *Rev. Mod. Phys.* 81, 163-234

Liu, H. J., Chen, G. F., Zhao, W., Wang, Y. S., Wang, T. & Zhao, S. H. (2001), Phase matching analysis of noncollinear optical parametric process in nonlinear anisotropic crystals, *Opt. Commun.* 197, 507–514

Meckel, M., Comtois, D., Zeidler, D., Staudte, A., Pavičić, D., Bandulet, H. C., Pépin, H., Kieffer, J. C., Dörner, R., Villeneuve, D. M. & Corkum, P. B. (2008), Laser-Induced Electron Tunneling and Diffraction, *Science* 320, 1478-1482

Miaja-Avila, L., Saathoff, G., Mathias, S., Yin, J., La-o-vorakiat, C., Bauer, M., Aeschlimann, M., Murnane, M. M. & Kapteyn, H. C. (2008), Direct Measurement of Core-Level Relaxation Dynamics on a Surface-Adsorbate System, *Phys. Rev. Lett.* 101, 046101-1-4

Moses, J., Huang, S.-W., Hong, K.-H., Mücke, O. D., Falcão-Filho, E. L., Benedick, A., Ilday, F. Ö., Dergachev, A., Bolger, J. A., Eggleton, B. J. & Kärtner, F. X. (2009), Highly stable ultrabroadband mid-IR optical parametric chirped-pulse amplifier optimized for superfluorescence suppression, *Opt. Lett.* 34, 1639-1641

Mücke, O. D., Sidorov, D., Dombi, P., Pugžlys, A., Baltuška, A., Ališauskas, S., Smilgevičius, V., Pocius, J., Giniūnas, L., Danielius, R. & Forget, N. (2009a), Scalable Yb-MOPA-driven carrier-envelope phase-stable few-cycle parametric amplifier at 1.5 μm, *Opt. Lett.* 34, 118-120

Mücke, O. D., Ališauskas, S., Verhoef, A. J., Pugžlys, A., Baltuška, A., Smilgevičius, V., Pocius, J., Giniūnas, L., Danielius, R. & Forget, N. (2009b), Self-compression of millijoule 1.5 μm pulses, *Opt. Lett.* 34, 2498-2500

Nejadmalayeri, A. H., Herman, P. R., Burghoff, J., Will, M., Nolte, S. & Tünnermann, A. (2005), Inscription of optical waveguides in crystalline silicon by mid-infrared femtosecond laser pulses, *Opt. Lett.* 30, 964-966

Nisoli, M., De Silvestri, S. & Svelto, O. (1996), Generation of high energy 10 fs pulses by a new pulse compression technique, *Appl. Phys. Lett.* 68, 2793-2795

Nisoli, M., De Silvestri, S., Svelto, O., Szipöcs, R., Ferencz, K., Spielmann, C., Sartania, S. & Krausz, F. (1997), Compression of high-energy laser pulses below 5 fs, *Opt. Lett.* 22, 522-524

Paye, J. (1992), The Chronocyclic Representation of Ultrashort Light Pulses, *IEEE J. Quantum Electron.* 28, 2262-2273

Pérez-Hernández, J. A., Roso, L. & Plaja, L. (2009), Harmonic generation beyond the Strong-Field Approximation: the physics behind the short-wave-infrared scaling laws, *Opt. Express* 17, 9891-9903

Popmintchev, T., Chen, M.-C., Cohen, O., Grisham, M. E., Rocca, J. J., Murnane, M. M. & Kapteyn, H. C. (2008), Extended phase matching of high harmonics driven by mid-infrared light, *Opt. Lett.* 33, 2128-2130

Popmintchev, T., Chen, M.-C., Bahabad, A., Gerrity, M., Sidorenko, P., Cohen, O., Christov, I. P., Murnane, M. M. & Kapteyn, H. C. (2009), Phase matching of high harmonic generation in the soft and hard X-ray regions of the spectrum, *Proc. Natl. Acad. Sci. USA* 106, 10516–10521

Sansone, G., Benedetti, E., Calegari, F., Vozzi, C., Avaldi, L., Flammini, R., Poletto, L., Villoresi, P., Altucci, C., Velotta, R., Stagira, S., De Silvestri, S. & Nisoli, M. (2006), Isolated Single-Cycle Attosecond Pulses, *Science* 314, 443-446

Schiessl, K., Ishikawa, K. L., Persson, E. & Burgdörfer, J. (2007), Quantum Path Interference in the Wavelength Dependence of High-Harmonic Generation, *Phys. Rev. Lett.* 99, 253903-1-4

Seres, J., Seres, E., Verhoef, A. J., Tempea, G., Streli, C., Wobrauschek, P., Yakovlev, V., Scrinzi, A., Spielmann, C. & Krausz, F. (2005), Source of coherent kiloelectronvolt X-rays, *Nature* 433, 596

Shan, B. & Chang, Z. (2001), Dramatic extension of the high-order harmonic cutoff by using a long-wavelength driving field, *Phys. Rev. A* 65, 011804(R)-1-4

Sheehy, B., Martin, J. D. D., DiMauro, L. F., Agostini, P., Schafer, K. J., Gaarde, M. B. & Kulander, K. C. (1999), High Harmonic Generation at Long Wavelengths, *Phys. Rev. Lett.* 83, 5270-5273

Shiner, A. D., Trallero-Herrero, C., Kajumba, N., Bandulet, H.-C., Comtois, D., Légaré, F., Giguère, M., Kieffer, J.-C., Corkum, P. B. & Villeneuve, D. M. (2009), Wavelength Scaling of High Harmonic Generation Efficiency, *Phys. Rev. Lett.* 103, 073902-1-4

Stibenz, G., Zhavoronkov, N. & Steinmeyer, G. (2006), Self-compression of millijoule pulses to 7.8 fs duration in a white-light filament, *Opt. Lett.* 31, 274-276

Suda, A., Hatayama, M., Nagasaka, K. & Midorikawa, K. (2005), Generation of sub-10-fs, 5-mJ-optical pulses using a hollow fiber with a pressure gradient, *Appl. Phys. Lett.* 86, 111116-1-3

Takahashi, E. J., Kanai, T., Nabekawa, Y. & Midorikawa, K. (2008a), 10 mJ class femtosecond optical parametric amplifier for generating soft x-ray harmonics, *Appl. Phys. Lett.* 93, 041111-1-3

Takahashi, E. J., Kanai, T., Ishikawa, K. L., Nabekawa, Y. & Midorikawa, K. (2008b), Coherent Water Window X Ray by Phase-Matched High-Order Harmonic Generation in Neutral Media, *Phys. Rev. Lett.* 101, 253901-1-4

Tate, J., Auguste, T., Muller, H. G., Salières, P., Agostini, P. & DiMauro, L. F. (2007), Scaling of Wave-Packet Dynamics in an Intense Midinfrared Field, *Phys. Rev. Lett.* 98, 013901-1-4

Trisorio, A. & Hauri, C. P. (2007), Control and characterization of multiple circularly polarized femtosecond filaments in argon, *Opt. Lett.* 32, 1650-1652

Varanavičius, A., Dubietis, A., Beržanskis, A., Danielius, R. & Piskarskas, A. (1997), Near-degenerate cascaded four-wave mixing in an optical parametric amplifier, *Opt. Lett.* 22, 1603-1605

Varela, O., Zaïr, A., San Román, J., Alonso, B., Sola, I. J., Prieto, C. & Roso, L. (2009), Above-millijoule super-continuum generation using polarisation dependent filamentation in atoms and molecules, *Opt. Express* 17, 3630-3639

Verluise, F., Laude, V., Huignard, J.-P., Tournois, P. & Migus, A. (2000), Arbitrary dispersion control of ultrashort optical pulses with acoustic waves, *J. Opt. Soc. Am. B* 17, 138-145

Vozzi, C., Cirmi, G., Manzoni, C., Benedetti, E., Calegari, F., Sansone, G., Stagira, S., Svelto, O., De Silvestri, S., Nisoli, M. & Cerullo, G. (2006), High-energy, few-optical-cycle pulses at 1.5 μm with passive carrier-envelope phase stabilization, *Opt. Express* 14, 10109-10116

Vozzi, C., Calegari, F., Benedetti, E., Gasilov, S., Sansone, G., Cerullo, G., Nisoli, M., De Silvestri, S. & Stagira, S. (2007), Millijoule-level phase-stabilized few-optical-cycle infrared parametric source, *Opt. Lett.* 32, 2957-2959

Vozzi, C., Calegari, F., Frassetto, F., Poletto, L., Sansone, G., Villoresi, P., Nisoli, M., De Silvestri, S. & Stagira, S. (2009), Coherent continuum generation above 100 eV driven by an ir parametric source in a two-color scheme, *Phys. Rev. A* 79, 033842-1-6

Yakovlev, V. S., Ivanov, M. & Krausz, F. (2007), Enhanced phase-matching for generation of soft X-ray harmonics and attosecond pulses in atomic gases, *Opt. Express* 15, 15351-15364

Zilkie, A. J., Meier, J., Smith, P. W. E., Mojahedi, M., Aitchison, J. S., Poole, P. J., Allen, C. N., Barrios, P. & Poitras, D. (2006), Femtosecond gain and index dynamics in an InAs/InGaAsP quantum dot amplifier operating at 1.55 μm, *Opt. Express* 14, 11453-11459

Advances in Solid State Lasers Development and Applications

Edited by Mikhail Grishin

ISBN 978-953-7619-80-0
Hard cover, 630 pages
Publisher InTech
Published online 01, February, 2010
Published in print edition February, 2010

Invention of the solid-state laser has initiated the beginning of the laser era. Performance of solid-state lasers improved amazingly during five decades. Nowadays, solid-state lasers remain one of the most rapidly developing branches of laser science and become an increasingly important tool for modern technology. This book represents a selection of chapters exhibiting various investigation directions in the field of solid-state lasers and the cutting edge of related applications. The materials are contributed by leading researchers and each chapter represents a comprehensive study reflecting advances in modern laser physics. Considered topics are intended to meet the needs of both specialists in laser system design and those who use laser techniques in fundamental science and applied research. This book is the result of efforts of experts from different countries. I would like to acknowledge the authors for their contribution to the book. I also wish to acknowledge Vedran Kordic for indispensable technical assistance in the book preparation and publishing.

How to reference

In order to correctly reference this scholarly work, feel free to copy and paste the following:

O. D. Mücke, S. Ališauskas, A. J. Verhoef, A. Pugžlys, A. Baltuška, V. Smilgevičius, J. Pocius, L. Giniūnas, R. Danielius, and N. Forget (2010). Toward TW-Peak-Power Single-Cycle IR Fields for Attosecond Physics and High-Field Science, Advances in Solid State Lasers Development and Applications, Mikhail Grishin (Ed.), ISBN: 978-953-7619-80-0, InTech, Available from: http://www.intechopen.com/books/advances-in-solid-state-lasers-development-and-applications/toward-tw-peak-power-single-cycle-ir-fields-for-attosecond-physics-and-high-field-science

INTECH
open science | open minds

InTech Europe
University Campus STeP Ri
Slavka Krautzeka 83/A
51000 Rijeka, Croatia
Phone: +385 (51) 770 447
Fax: +385 (51) 686 166
www.intechopen.com

InTech China
Unit 405, Office Block, Hotel Equatorial Shanghai
No.65, Yan An Road (West), Shanghai, 200040, China
中国上海市延安西路65号上海国际贵都大饭店办公楼405单元
Phone: +86-21-62489820
Fax: +86-21-62489821

IntechOpen